Quantum Fluctuations and Excitations in Antiferromagnetic Quasicrystals

Stefan Wessel[(1)] and Igor Milat[(2)]
[(1)] *Institut für Theoretische Physik III, Universität Stuttgart, 70550 Stuttgart, Germany and*
[(2)] *Theoretische Physik, ETH Zürich, CH-8093 Zürich, Switzerland*
(Dated: October 8, 2004)

We study the effects of quantum fluctuations and the excitation spectrum for the antiferromagnetic Heisenberg model on a two-dimensional quasicrystal, by numerically solving linear spin-wave theory on finite approximants of the octagonal tiling. Previous quantum Monte Carlo results for the distribution of local staggered magnetic moments and the static spin structure factor are reproduced well within this approximate scheme. Furthermore, the magnetic excitation spectrum consists of magnon-like low-energy modes, as well as dispersionless high-energy states of multifractal nature. The dynamical spin structure factor, accessible to inelastic neutron scattering, exhibits linear-soft modes at low energies, self-similar structures with bifurcations emerging at intermediate energies, and flat bands in high-energy regions. We find that the distribution of local staggered moments stemming from the inhomogeneity of the quasiperiodic structure leads to a characteristic energy spread in the local dynamical spin susceptibility, implying distinct nuclear magnetic resonance spectra, specific for different local environments.

PACS numbers: 03.75.Hh,03.75.Lm,05.30.Jp

arXiv:cond-mat/0410180 v1 7 Oct 2004

I. INTRODUCTION

Quantum fluctuations are responsible for various degrees of disorder in low-dimensional quantum antiferromagnets. In particular two-dimensional systems show a variety of quantum disordered phases, competing with conventional long-range magnetic order. For example, while the Heisenberg model on the square lattice exhibits true long-range order at zero temperature[1], spatial inhomogeneous magnetic exchange eventually leads to a complete suppression of magnetic order in structures such as the plaquette lattice, driven by local singlet formation[2,3]. Other sources of magnetic disorder are frustration effects due to competing interactions[4], and site/bond depletion[5], where the reduction in the long-range magnetic order is accomplished by proliferation of localized low-energy excitations[6]. All these systems share the translational invariance of the underlying lattice structure - assuming sufficient self averaging in the case of quenched disorder.

Quasiperiodic systems, lacking translational symmetry in addition to their inhomogeneous lattice structure were initially thought to not support sizeable correlations of localized magnetic moments. However, recent neutron scattering experiments on Zn-Hg-Ho[7] as well as Cd-Mg-Tb[8] icosahedral quasicrystals support the presence of significant magnetic correlations in these three-dimensional quasicrystalline compounds, with the absence of true long-range magnetic order[9] due to large frustrations in the antiferromagnetic exchange[10].

Bipartite, and thus unfrustrated, quasiperiodic crystal structures were indeed shown to allow for sizeable two-sublattice antiferromagnetic order in a recent quantum Monte Carlo study of the spin-1/2 Heisenberg model on the octagonal tiling[10]. Furthermore, the magnetic order in this two-dimensional system was found to exhibit nontrivial patterns in the local staggered moment distribution, reflecting the self-similarity of the underlying quasiperiodic lattice structure[10]. A renormalization group approach based on this self-similarity indeed gives a gross account on the observed spread in the staggered magnetization[11]. Furthermore, the static spin structure factor exhibits magnetic selection rules that impose a shift of reciprocal space indices[10]. The resulting neutron diffraction pattern[10] can be accounted for by analysis[12] of the quasicrystal spin group[13], also applicable to frustrated classical models on the octagonal tiling with long-range exchange interactions[14].

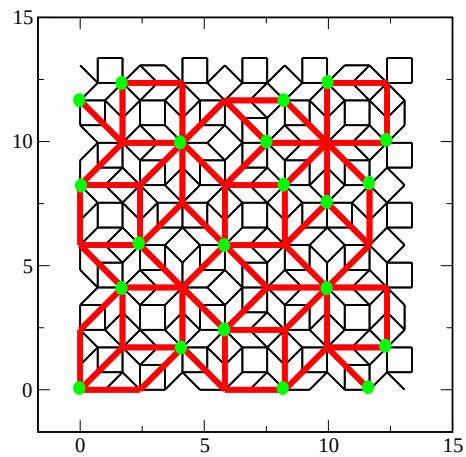

FIG. 1: Finite approximant of the octagonal tiling with 239 sites (thin lines), along with a superimposed inflated 41 sites approximant (thick lines) of rescaled edge length by a factor of $\lambda = 1 + \sqrt{2}$. For the 41 sites approximant the vertices of one of the two sublattices are dressed with a disk to exhibit the bipartite nature of the octagonal tiling.

While static properties of the Heisenberg antiferromagnet on the octagonal tiling are thus well studied, little is known about the spectral properties of these systems.

On general grounds one would expect gapless Goldstone-modes to dominate at low-energies, even though the translational symmetry is absent. In addition, one would expect to find multifractional eigenstates, as observed in tight-binding models on quasiperiodic lattices[15]. Here, we investigate dynamical properties of quantum magnetic quasicrystals in order to identify the relevant energy scales of quantum fluctuations in such systems, determine the magnetic excitation spectrum, as well as to provide theoretical grounds for future experiments on magnetic quasicrystals, such as inelastic neutron scattering or magnetic resonance. In particular, we use linear spin-wave theory, which was successfully used in studies of periodic magnetically ordered systems, and apply it to the quasiperiodic case.

The outline of the paper is as follows: Basic properties of the octagonal tiling are presented in the following section. In Sec. III we review linear spin wave theory in a real space formulation, and present a numerical construction of the eigenmode expansion. An alternative scheme is given in the Appendix. The results of applying this method to the octagonal tiling are discussed in Sec. IV: In Sec. IV A we discuss static properties of the magnetic correlations on the octagonal tiling, and compare our results to previous quantum Monte Carlo simulations. A detailed analysis of the excitation spectrum is presented in Sec. IV B, followed by a discussion of dynamical magnetic properties, such as the dynamical spin structure factor in Sec. IV C, and the local dynamical spin susceptibility (Sec. IV D). Finally, we conclude in Sec. V with a perspective on future investigations.

II. OCTAGONAL TILING

In the following, we analyze the magnetic ground state properties and excitation spectrum of the nearest-neighbor antiferromagnetic spin$-1/2$ Heisenberg model,

$$H = J \sum_{\langle i,j \rangle} \mathbf{S}_i \cdot \mathbf{S}_j, \quad J > 0, \tag{1}$$

on the most prominent example of a magnetic quasicrystal in two dimensions, the octagonal tiling. The octagonal tiling is a bipartite quasiperiodic crystal system, and possesses an overall eightfold rotational symmetry, allowing for simple two-sublattice antiferromagnetism[12]. Sites in this tiling have coordination numbers z ranging from 3 to 8, leading to a broad distribution of local staggered moments in the magnetically ordered ground state[10]. A further important property of the octagonal tiling, in the absence of translational invariance, is its self-similarity under inflation transformations[16]. This reversible operation refers to a well-defined decimation of a subset of vertices of the tiling, followed by a re-connection of the new vertices. Aside from a trivial rescaling of the length scale by a factor $\lambda = 1 + \sqrt{2}$, the infinite quasicrystal is left unchanged by this transformation.

For our numerical study we consider finite square approximants of the octagonal tiling with 41, 239, and 1393 sites. These approximants can be obtained by the "cut-and-project" method from a four-dimensional cubic lattice[18], and are related by the inflation transformation, an example of which is shown in Fig. 1. In order to avoid boundary-induced frustration effects, we apply toroidal boundary conditions[19]. Due to the lack of translational symmetry, we thus need to solve real-space linear spin-wave theory on lattices with up to 5572 sites. Before presenting our results, we provide details about the numerical scheme used in our calculations in the following section.

III. NUMERICAL SPIN-WAVE APPROXIMATION

In this section, we review linear spin-wave theory, applied to the antiferromagnetic Heisenberg model on finite, bipartite lattices. We consider a bipartite lattice with sublattices A and B consisting of N_A and N_B sites, respectively. For the octagonal approximants considered in this work $N_A = N_B$, however the following approach also applies if N_A and N_B are different. Following the standard Holstein-Primakoff approach[20], we represent the spins in terms of bosonic operators a_i and b_i. For $i \in A$,

$$\begin{aligned} S_i^z &= S - a_i^\dagger a_i, \\ S_i^+ &= \sqrt{2S}\left(1 - \frac{a_i^\dagger a_i}{2S}\right)^{1/2} a_i, \\ S_i^- &= \sqrt{2S} a_i^\dagger \left(1 - \frac{a_i^\dagger a_i}{2S}\right)^{1/2}, \end{aligned} \tag{2}$$

where S denotes the spin magnitude, and

$$\begin{aligned} S_j^z &= -S + b_j^\dagger b_j, \\ S_j^+ &= \sqrt{2S} b_j^\dagger \left(1 - \frac{b_j^\dagger b_j}{2S}\right)^{1/2}, \\ S_j^- &= \sqrt{2S}\left(1 - \frac{b_j^\dagger b_j}{2S}\right)^{1/2} b_j, \end{aligned} \tag{3}$$

for $j \in B$. The linear spin-wave Hamiltonian is obtained by substituting the above identities in Eq. (1), expanding the square roots in of $1/S$, and keeping terms of lowest order $(1/S)^0$,

$$H_{SW} = -JS(S+1)N_b + JSH_2, \tag{4}$$

$$H_2 = \sum_{\langle i,j \rangle} \left(a_i^\dagger a_i + b_j b_j^\dagger + a_i^\dagger b_j^\dagger + b_j a_i \right), \tag{5}$$

where N_b denotes the number of bonds, and the sum in H_2 extends over all bonds of the bipartite lattice. Introducing the $N_s = N_A + N_B$ component row vector

$$\bar{a}^\dagger = (a_1^\dagger, ..., a_{N_A}^\dagger, b_1, ..., b_{N_B}), \tag{6}$$

and the corresponding columnar conjugate, we can express the quadratic part of the Hamiltonian in matrix notation,

$$H_2 = \bar{a}^\dagger M \bar{a} = \sum_{\langle i,j \rangle} \bar{a}^\dagger M^{(i,j)} \bar{a}, \tag{7}$$

where

$$\begin{aligned} \left(M^{(i,j)}\right)_{k,l} &= \delta_{i,k}\delta_{i,l} + \delta_{j+N_A,k}\delta_{j+N_A,l} \\ &\quad + \delta_{i,k}\delta_{j+N_A,l} + \delta_{j+N_A,k}\delta_{i,l} \end{aligned} \tag{8}$$

is the connectivity matrix of the lattice structure. The bipartiteness of the lattice thus allows for a direct formulation in terms of the $N_s \times N_s$ hermitian matrix M, instead of the general formulation based on a $2N_s \times 2N_s$ matrix[21]. We now seek a Bogoliubov transformation to the N_n normal bosonic modes β_k, such that the spin-wave Hamiltonian H_{SW} is diagonal when expressed in terms of the β_k,

$$H_{SW} = N_s E_0 + \sum_{k=1}^{N_n} \omega_k \beta_k^\dagger \beta_k, \tag{9}$$

where $\omega_k > 0$ denotes the eigenfrequency of the k-th mode, and E_0 the ground state energy per site. To this end we make an Ansatz,

$$\bar{a} = T\bar{\beta}, \tag{10}$$

with

$$\bar{\beta}^\dagger = (\beta_1^\dagger, ..., \beta_{N_+}^\dagger, \beta_{N_++1}, ..., \beta_{N_n}), \tag{11}$$

so that we divide the N_n normal bosonic modes into two disjunct sets of length N_+, and $N_- = N_n - N_+$, respectively, further determined below. Due to the bosonic commutation relations, the transformation T has to fulfill

$$T\Gamma T^\dagger = \Sigma, \tag{12}$$

with matrices Γ and Σ, defined by

$$\Gamma = \begin{pmatrix} 1_{N_+} & 0 \\ 0 & -1_{N_-} \end{pmatrix}, \quad \Sigma = \begin{pmatrix} 1_{N_A} & 0 \\ 0 & -1_{N_B} \end{pmatrix}. \tag{13}$$

Here, 1_N denotes the $N \times N$ identity matrix[17]. Since $\Sigma^2 = 1$, as well as $\Gamma^2 = 1$, and because the left and right inverse of a square matrix are identical, if T satisfies

$$T^\dagger \Sigma T = \Gamma, \tag{14}$$

the bosonic commutation relations are fulfilled. Since T diagonalizes H_2, we have

$$T^\dagger M T = \Omega, \quad \Omega = \mathrm{diag}(\omega_1, ..., \omega_{N_n}), \tag{15}$$

from which we find upon multiplication from the left with $T\Gamma$, that T has to satisfy

$$\Sigma M T = T\Gamma\Omega. \tag{16}$$

The column vectors of T are thus seen to be related to the right eigenvectors of ΣM. For semi-positive M, ΣM has real eigenvalues, and eigenvectors belonging to different eigenvalues are orthogonal[21]. We denote the number of positive (negative) eigenvalues by N_+ (N_-), the number of zero-modes by N_0, and label the positive (negative) eigenvalues by λ_i^+, $i = 1, ..., N_+$ (λ_i^-, $i = 1, ..., N_-$). After numerically solving the non-hermitian $N_s \times N_s$ eigenvalue problem for ΣM[22], we construct within the subspace of each degenerate eigenvalue $\lambda_n^\pm > 0 (< 0)$ of dimension $d_n^\pm$ eigenvectors $z_{n,1}^\pm, ..., z_{m,d_n^\pm}^\pm$, obeying

$$(z_{n,i}^\pm)^\dagger \Sigma z_{n,j}^\pm = \pm\delta_{i,j}, \quad i,j = 1, ..., d_n^\pm \tag{17}$$

using Gram-Schmidt orthogonalization with respect to Σ (ref. 23). We then obtain T from the orthonormal eigenvectors as

$$T = (z_{1,1}^+, ..., z_{N_+,d_{N_+}^+}^+, z_{1,d_1}^-, ..., z_{N_-,d_{N_-}^-}^-), \tag{18}$$

where Eq. (17) ensures that Eq. (14) is satisfied. The corresponding eigenfrequencies are given by

$$\omega_k = JS\lambda_i^+, \quad k = 1, ..., N_+, \tag{19}$$

$$\omega_{N_++k} = -JS\lambda_k^-, \quad k = 1, ..., N_-. \tag{20}$$

The zero-modes of ΣM correspond to collective modes due to the broken continuous symmetry implied by the classical Néel state[6,21]. Furthermore, the ground state energy becomes

$$E_0 N_s = -JS(S+1)N_b + JS\sum_{k=1}^{N_-} |\lambda_k^-|. \tag{21}$$

An alternative means of numerically constructing the transformation matrix T is presented in the appendix. We have verified, that both approaches indeed yield the same results.

IV. RESULTS

In this section, we present the results obtained by applying the linear spin-wave approximation to the octagonal tiling introduced in Sec. II. Within linear spin-wave theory, ground state expectation values of both static and dynamic magnetic correlations can be calculated from contractions of bosonic normal mode operators. It turns out convenient for this purpose, to express the Bogoliubov transformation in terms of the row vectors

$$\begin{aligned} \tilde{a}^\dagger &= (a_1^\dagger, ..., a_{N_A}^\dagger, b_1^\dagger, ..., b_{N_B}^\dagger, a_1, ..., a_{N_A}, b_1, ..., b_{N_B}), \\ \tilde{\beta}^\dagger &= (\beta_1^\dagger, ..., \beta_{N_n}^\dagger, \beta_1, ..., \beta_{N_n}), \end{aligned}$$

as

$$\tilde{a} = \tilde{T}\tilde{\beta}, \quad \tilde{T} = \begin{pmatrix} U & V \\ V^* & U^* \end{pmatrix}. \tag{22}$$

One obtains U and V from the transformation matrix T of Eq. (10), upon defining $N_+ \times N_+$ matrices A and B, and $N_- \times N_-$ matrices C and D such that

$$T = \begin{pmatrix} A & C \\ B & D \end{pmatrix}, \tag{23}$$

and gets

$$U = \begin{pmatrix} A & 0 \\ 0 & D^* \end{pmatrix}, \quad V = \begin{pmatrix} 0 & C \\ B^* & 0 \end{pmatrix}. \tag{24}$$

A. Staggered magnetization

In this section we examine static properties of the magnetic ground state in the octagonal tiling. For this purpose, we first calculate the staggered magnetization at each lattice site i in linear spin-wave theory,

$$m_s(i) = |\langle S_i^z \rangle| = S - \sum_k |V_{ik}|^2. \tag{25}$$

The spatially averaged staggered magnetization

$$m_s = \sum_{i=1}^{N_s} m_s(i) \tag{26}$$

is shown as a function of the system size N_s of the approximant of the octagonal tiling in Fig. 2. The finite size values scale well as a function of $N_s^{-1/2}$, and indicate a sizeable staggered magnetization of the long ranged ordered ground state in the octagonal tiling. The value of m_s extrapolated to the thermodynamic limit is $m_s = 0.34$, and agrees well with the quantum Monte Carlo result, $m_s = 0.337 \pm 0.002$[10]. The weak reduction of the order parameter by quantum fluctuations is indicative for the feasibility of the linear spin-wave approach in this system. The ground state energy E_0, shown in the inset of Fig. 2, is also found to scale well as a function of $N_s^{-3/2}$, as expected for an ordered state[24]. The extrapolated value in the thermodynamic limit, $E_0 = -0.646$, compares well with the quantum Monte Carlo result, $E_0 = -0.6581(1)$[25].

In Ref. 10, the magnetic ground state on the octagonal tiling was found to exhibit a nontrivial local structure reflecting the self-similarity of the underlying quasiperiodic lattice structure. We now analyze to what extent spin-wave theory is able to reproduce this structure and thus to account for the specific nature of quantum fluctuations in an inhomogeneous connectivity. For this purpose, we show in Fig. 3 the linear spin-wave results of the local staggered magnetization, $m_s(i)$, for the 1393 sites approximant, and compare those with values grouped according to the coordination number z of the various sites, with the quantum Monte Carlo data of Ref. 10.

We find linear spin-wave theory to qualitatively reproduce characteristic features of the local staggered moment distribution, such as (i) a wide spread of the moments, in particular for small values of z, (ii) a prominent

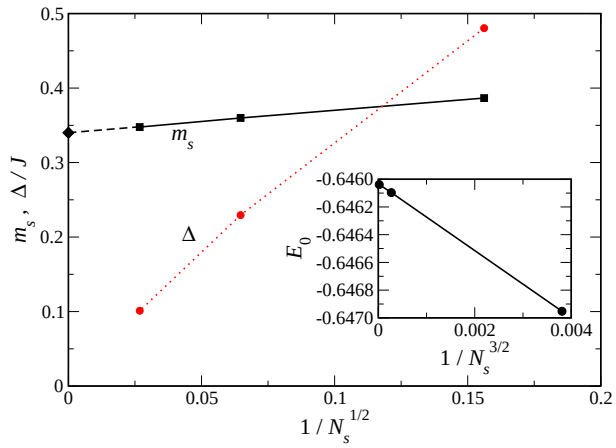

FIG. 2: Finite size scaling of the ground state staggered magnetization, m_s, and the lowest excitation gap, Δ, for the $S = 1/2$ Heisenberg model on the octagonal tiling in linear spin-wave theory. The inset shows the finite size scaling of the ground state energy, E_0, for the same system.

bimodal splitting of the moments for $z = 5$ and (iii) the hierarchical structure observed in the splitting of the moments for sites with $z = 8$, shown in the inset of Fig. 3. These splittings in the local staggered moments can be accounted for by the properties of inequivalent sites under deflation transformations, reflecting their different local environments[10]. In particular, fivefold sites with $z = 5$ always occur in pairs, with two different types of site. The first type is connected to four fourfold ($z = 4$) sites and the other fivefold site, while for the other type two neighbors are fourfold, two threefold ($z = 3$) and one fivefold. This difference in the local connectivity leads to the observed splitting[10], and is also reflected in a different behavior of the two types of fivefold sites under deflation transformations: while one type is decimated, the other remains as a threefold site in the deflated tiling. The eightfold ($z = 8$) sites exhibit an even richer, hierarchical structure shown in the inset of Fig. 3, with moments grouped according to the different deflation properties of the eightfold sites, namely their new coordination number z'. The high symmetry sites with $z' = 8$ show a further hyperfine splitting, with moments grouped according to the value of z'' under a second deflation, indicated by numbers next to the symbols in the inset of Fig. 3. As discussed in Ref. 10, these splittings eventually lead to a multifractal distribution of local staggered moments in the infinite quasicrystal, for this class of sites.

From a quantitative comparison of the local staggered magnetization between linear spin-wave theory and quantum Monte Carlo, we find characteristic limitations of the spin-wave approach to persist on a local level. Namely, while local staggered moments of high-connectivity sites are reproduced even quantitatively, deviations of about 8% are observed for low-connectivity sites. In an inhomogeneous environment, linear spin-wave theory is thus

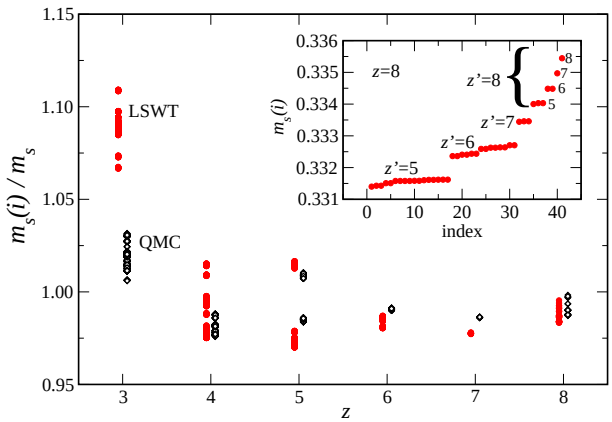

FIG. 3: Dependence of the local staggered magnetization on the coordination number z for all sites in the 1393 sites approximant of the octagonal tiling within linear spin-wave theory of the $S = 1/2$ Heisenberg model (LSWT). For reference, results of quantum Monte Carlo simulations of the same system (QMC) are also shown[10]. The inset exhibits the hierarchy of the local staggered magnetization of the $z = 8$ sites, grouped according to the value of z' under a deflation transformation. Numbers next to symbols give the value of z'' for $z' = 8$ sites under a further deflation.

more accurate at sites of large coordination, as might have been expected from its behavior in homogenous systems.

The long-range antiferromagnetic order in the octagonal tiling leads to characteristic neutron diffraction patterns, due to selection rules imposed by the magnetic symmetry[10,12]. These patterns can be obtained from the static longitudinal structure factor

$$S^{\parallel}(\mathbf{k}) = \sum_{i,j=1}^{N_s} e^{i\mathbf{k}\cdot(\mathbf{r}_i - \mathbf{r}_j)} \langle S_i^z S_j^z \rangle, \tag{27}$$

which within linear spin-wave theory amounts to the Fourier transform of the real space distribution of $\langle S_i^z \rangle$. Since linear spin-wave theory reproduces the spatial staggered moment distribution rather well, as seen from Fig. 3, the resulting static longitudinal structure factor, shown in the left of Fig. 4 also compares well to the quantum Monte Carlo result[10]. In particular, it exhibits the extinction of nuclear Bragg peaks and the emergence of new, magnetic Bragg peaks. For a detailed theoretical derivation of the various selection rules in the octagonal tiling, we refer to the explicit enumerations in Ref. 12.

The structural distribution of local staggered moments observed in Fig. 3 exhibits an inhomogeneous distribution of quantum fluctuations. As seen from Eq. (25), fluctuations in m_s arise from distinct contributions from the various eigenstates of the system. To quantify the relevance of the different eigenstates for the quantum fluctuations, we study the reduction of the staggered magnetization at each lattice site i, which can be parameterized as a

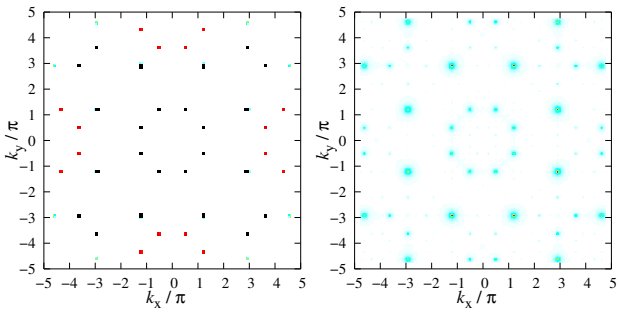

FIG. 4: Intensity plot of the static longitudinal magnetic structure factor $S^{\parallel}(\mathbf{k})$ (left), and the integrated dynamical spin structure factor $S^{\perp}(\mathbf{k})$ (right) for the $S = 1/2$ Heisenberg antiferromagnet on the 1393 sites approximant of the octagonal tiling.

function of energy,

$$\delta m_s(i, \omega) = \frac{\sum_k |V_{ik}|^2 \delta(\omega - \omega_k)}{\sum_k \delta(\omega - \omega_k)}. \tag{28}$$

In Fig. 5 we show $\delta m_s(i, \omega)$, averaged separately over sites with $z = 3$, and $z = 8$.[26]

In both cases, the dominant contribution to quantum fluctuations stem from the low-energy modes, with $\omega/JS < 2$. For threefold sites, further contributions to δm_s arise from higher energy modes, which are not relevant for the eightfold sites. In general, we find the upper bound of the energy range that is relevant for quantum fluctuations to decrease with increasing coordination number z. Although sites with low coordination numbers thus receive quantum fluctuations over a larger range in energy space, their staggered moment is typically larger than for high coordinated sites, as seen from Fig. 3. A transfer of relevant quantum fluctuations to low-energy modes is thus responsible for a decrease of the staggered moment at specific sites. This increased relevance of low-energy modes for quantum fluctuations is also observed for sites with the same coordination number. For example, the inset of Fig. 5 shows δm_s for the fivefold sites, where the bimodal splitting was observed in Fig. 3, averaged separately over sites with a small and a large moment, respectively. The additional reduction of the local moment for one type of fivefold sites is clearly seen to be due to a proliferation of quantum fluctuations in the lower energy region.

This hints at a close link between the structure of the inhomogeneous magnetic ground state and the magnetic excitation spectrum. In the following subsection, we proceed to analyze the magnetic excitations in more detail.

B. Excitation Spectrum

In the previous section we found that spin-wave theory provides a qualitative, and even quantitative account on

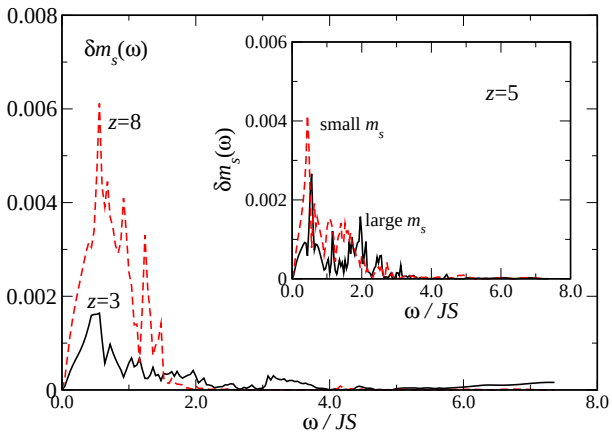

FIG. 5: Frequency dependence of quantum fluctuations to the staggered magnetization, $\delta m_s(\omega)$, for the $S = 1/2$ Heisenberg model on the octagonal tiling, averaged separately over sites with coordination numbers $z = 3$ and 8. The inset shows $\delta m_s(\omega)$ for $z = 5$, averaged separately over sites with a small and large staggered magnetization, respectively.

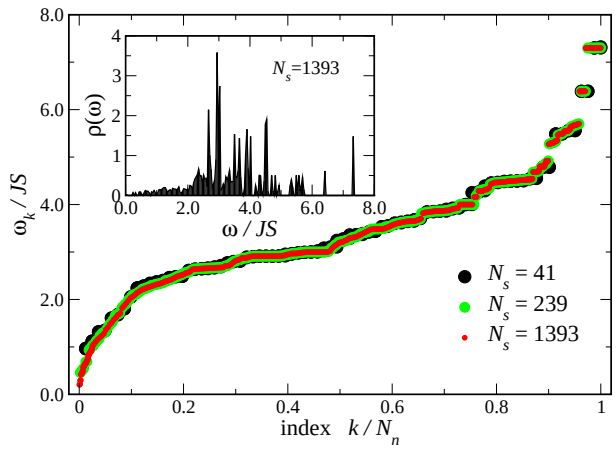

FIG. 6: Excitation spectra of the Heisenberg antiferromagnet on finite approximants of the octagonal tiling of different sizes within linear spin-wave theory. The inset shows the density of state, $\rho(\omega)$, for the largest approximant.

the magnetic ground state properties of the Heisenberg model on the octagonal tiling. We now proceed to use linear spin-wave theory to gain insights into the spectral properties of this quasiperiodic antiferromagnet.

The spectra of spin-wave normal modes for the first three approximants of the octagonal tiling are shown in Fig. 6. For finite approximants the spectra consists of discrete sets of energy levels, spanning an extended range up to $\omega_{max}/JS \approx 7.3$. This implies a bandwidth almost a factor two larger than for the Heisenberg model on the square lattice, where $\omega_{max}/JS = 4$. Upon increasing the system size, the energy spectrum appears to develop a dense band, and two isolated pockets at higher energies, near $\omega/JS \approx 6.5$ and 7.3, respectively. The presence of a third pocket near $\omega/JS \approx 5.5$ cannot be excluded from the finite size data. However, from Fig. 6 the gap near $\omega/JS \approx 5$ appears to eventually close for higher approximants, whereas the gaps to the higher energy pockets do not show any decrease for the approximants considered here.

For a more quantitative analysis of the distribution of normal modes, we calculate the density of states of the spin-wave excitation spectrum (DOS),

$$\rho(\omega) = \sum_k \delta(\omega - \omega_k), \tag{29}$$

shown for the largest approximant in the inset of Fig. 6. The spin-wave DOS exhibits a characteristic spiky shape in the high-energy regime, in particular for energies larger than $\omega/JS \approx 3$, similar to shapes found for the tight-binding Hamiltonian on the same lattice structure[27]. In the low-energy region, the DOS appears more smooth, with a residual roughness due to the limited resolution of the energy spectra due to finite size effects. We indeed find similar resolution limited roughness also on finite square lattice systems.

On general grounds, the presence of a long-range ordered ground state is expected to characterise the low-energy properties of the excitation spectrum. In particular, due to the broken $SU(2)$ symmetry, we expect the gap to the lowest excitation, Δ, to close in the thermodynamic limit of the quasiperiodic tiling. A finite size scaling analysis of Δ, shown in Fig. 2, is indeed consistent with $\Delta \propto N_s^{-\alpha}$, where $\alpha \approx 0.5$. At low energies the DOS furthermore increases linearly, $\rho(\omega) \propto \omega$, as seen from the quadratic low-energy behavior of the cumulative density of states,

$$N(\omega) = \int_0^\omega d\epsilon\, \rho(\epsilon), \tag{30}$$

shown in Fig. 7. Here, we employ $N(\omega)$, since this quantity is less susceptible to resolution limited roughness than $\rho(\omega)$, due to the frequency integration. The low-energy features of the spin-wave DOS in the octagonal tiling are also observed in periodic antiferromagnets. For example, on the square lattice, antiferromagnetic spin-waves obey a linear dispersion relation at low energies $\omega_{\mathbf{k}} \approx \sqrt{8}JS|\mathbf{k}|$, resulting in a linear low-energy DOS in this system.

The similarity of the low-energy DOS for the Heisenberg model on the quasiperiodic octagonal tiling to the periodic case suggest that the low-energy excitation could be delocalized, magnon-like modes also in the octagonal tiling. We are thus lead to analyze the spatial extent of the eigenstates found within linear spin-wave theory. An appropriate method to characterize the localization properties is the inverse participation ratio (IPR)[28] which expresses the spatial extent of the wavefunction of a given state. For the bosonic excitations of quantum magnets, the IPR of an eigenstate is given by its contribution to

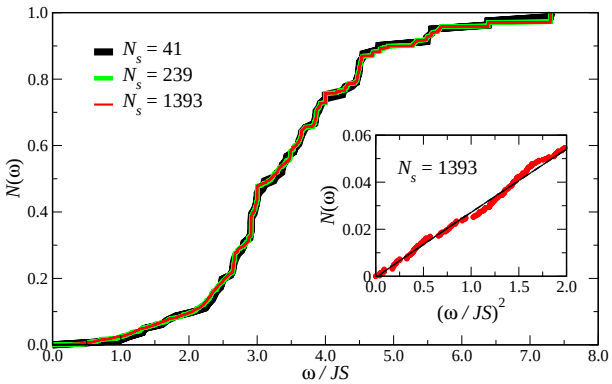

FIG. 7: Cumulative density of states, $N(\omega)$, of the Heisenberg antiferromagnet on finite approximants of the octagonal tiling of different sizes within linear spin-wave theory. The inset exhibits the quadratic scaling of $N(\omega)$ at low energies for the largest approximant, indicative of a linear low-energy density of states.

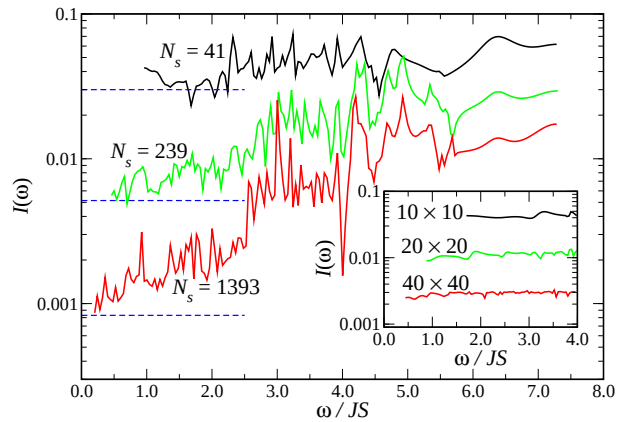

FIG. 8: Frequency dependent inverse participation ratio, $I(\omega)$, for the $S = 1/2$ Heisenberg antiferromagnet on finite approximants of the octagonal tiling of different sizes, obtained within linear spin-wave theory. Dashed lines indicate a finite size scaling as N_s^{-1}, expected for extended states. The inset shows linear spin-wave results for $I(\omega)$ on square lattices of different sizes.

the quantum fluctuations of the staggered magnetization. Following Ref. 6, we define the energy dependent inverse participation ratio

$$I(\omega) = \frac{\sum_k I_k \, \delta(\omega - \omega_k)}{\sum_k \delta(\omega - \omega_k)}, \tag{31}$$

where

$$I_k = \frac{\sum_i |V_{ik}|^4}{\left(\sum_i |V_{ik}|^2\right)^2}, \tag{32}$$

and study its scaling behavior upon increasing the system size. For delocalized states of a d dimensional quantum system, the IPR decreases with the system size, N_s, as N_s^{-1}. Exponentially localized states should be very insensitive to the system size and one expects a size independent IPR.

Fig. 8 shows the calculated IPR as a function of energy for the spin$-1/2$ Heisenberg model on finite approximants of the octagonal tiling. For comparison, we show in the inset the corresponding quantity for the Heisenberg model on the square lattice. In the square lattice case, all eigenstates show the characteristic N_s^{-1} scaling, expected for extended magnon states. For the octagonal tiling, we find such behavior only for the low-energy modes, but due to the limited resolution cannot exclude a reduced finite size scaling down to zero frequency. The low-energy modes in the octagonal tiling thus appear as extended excitations out of the antiferromagnetic ground state, similar to coherent magnons in the periodic case. The higher energy states also do not appear exponential localized, but show a significantly reduced finite size scaling $I(\omega) \propto N_s^{-\beta}$, with a scaling exponent $\beta < 1$, characteristic for multifractal states, as observed for critical states at the Anderson localization transition[29]. The effective exponent β decreases towards the upper edge of the spectrum, being lowest for energies near the isolated pockets found in the DOS in Fig. 6. While a reliable determination of β would require the study of substantially larger approximants, we estimate a value of $\beta \approx 0.2$ for the high-energy modes. The multifractality of eigenstates found in non-interacting models on quasiperiodic crystals[15] is thus clearly observed also for excitations of strongly correlated systems, such as the Heisenberg antiferromagnet.

C. Dynamical spin structure factor

Having analyzed the spin-wave excitations of the Heisenberg antiferromagnet on the octagonal tiling, we proceed to study magnetic properties exhibiting the magnetic excitation spectrum, such as the dynamical spin structure factor, and local dynamical spin susceptibility.

The dynamical spin structure factor, accessible experimentally by inelastic neutron scattering, reflects the time-dependent spin-spin correlation functions, transformed to momentum space,

$$S^{\perp}(\mathbf{k}, \omega) = \frac{1}{N_s} \sum_{i,j=1}^{N_s} e^{i\mathbf{k}\cdot(\mathbf{r}_i - \mathbf{r}_j)} S^{\perp}(i, j, \omega), \tag{33}$$

with

$$S^{\perp}(i, j, \omega) = \frac{1}{2} \int_{-\infty}^{\infty} dt \, e^{i\omega t} \langle S_i^+(t) S_j^-(0) + S_i^-(t) S_j^+(0) \rangle. \tag{34}$$

Using the normal-mode expansion, Eq. (22), we obtain the following expression for $S^{\perp}(i, j, \omega)$ within linear spin-wave theory,

$$S^{\perp}(i, j, \omega) = S \sum_k \left(U_{ik} U_{jk}^* + V_{ik}^* V_{jk} \right) \delta(\omega - \omega_k), \tag{35}$$

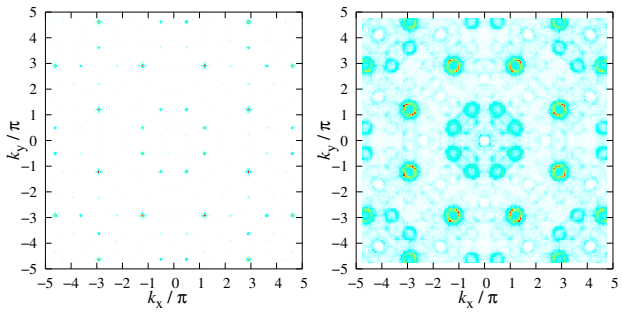

FIG. 9: Intensity plot of the dynamical spin structure factor, $S(\mathbf{k},\omega)$, for fixed $\omega/JS = 0$ (left) and $\omega/JS = 1.8$ (right) for the $S = 1/2$ Heisenberg antiferromagnet on the 1393 sites approximant of the octagonal tiling.

from which $S^{\perp}(\mathbf{k},\omega)$ is readily obtained using a fast Fourier transformation. Most spectral weight in $S^{\perp}(\mathbf{k},\omega)$ is located at momenta corresponding to magnetic Bragg peaks, as seen by comparing the integrated dynamical spin structure factor,

$$S^{\perp}(\mathbf{k}) = \int \frac{d\omega}{2\pi}\, S^{\perp}(\mathbf{k},\omega), \tag{36}$$

shown in the right of Fig. 4 to the static longitudinal structure factor, $S^{\parallel}(\mathbf{k})$, in the left of Fig. 4. For a detailed analysis of the dynamical spin structure factor, we consider both constant-frequency scans, shown in Figs. 9 to 12, as well as scans along various momentum space directions, shown in Figs. 13 and 14. To increase the contrast in these figures, we have rescaled the data to the maximum value in each plot, separately.

In order to compare the relative spectral weight at different energies, we show in Fig. 10 the momentum-integrated spectral function,

$$S^{\perp}(\omega) = \int \frac{d^2k}{(2\pi)^2}\, S(\mathbf{k},\omega). \tag{37}$$

Compared to the DOS, we find that apart from the low-energy region below $\omega/JS \approx 2$, the shape of $S^{\perp}(\omega)$ closely reflects the structures in the DOS. In the low-energy region, we observe an disproportionately large contribution to $S^{\perp}(\omega)$, in contrast to the low DOS in this region. The difference between $S^{\perp}(\omega)$, and the DOS, $\rho(\omega)$, in linear spin-wave theory is obtained using Eq. (22) as

$$S^{\perp}(\omega) - S\rho(\omega) = 2S \sum_{i,k} |V_{ik}|^2 \delta(\omega - \omega_k), \tag{38}$$

and indicates, that the extra contributions to $S^{\perp}(\omega)$ at energies $\omega/JS < 2$ are due to the spectral predominance of low energy quantum fluctuations, $\delta m_s(\omega)$, Eq. (28), shown in Fig. 5. In the following, we first consider the dynamical spin structure factor in this low-energy region, which is dominated by magnetic Bragg scattering.

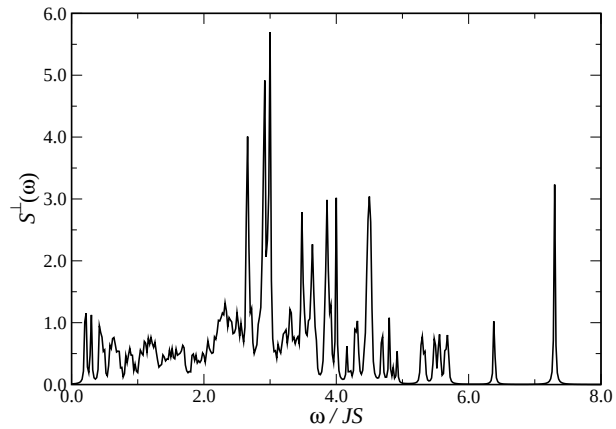

FIG. 10: Frequency dependence of the momentum-integrated dynamical spin structure factor, $S^{\perp}(\omega)$, for the $S = 1/2$ Heisenberg antiferromagnet on the octagonal tiling.

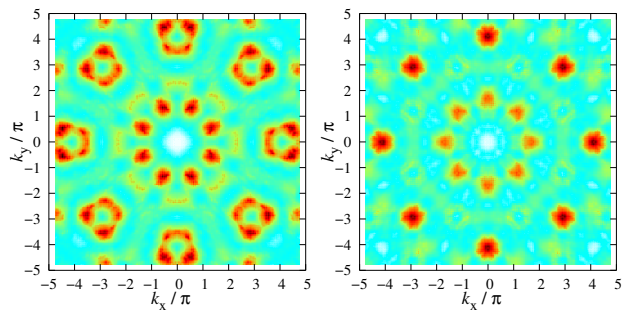

FIG. 11: Intensity plot of the dynamical spin structure factor, $S(\mathbf{k},\omega)$, for fixed $\omega/JS = 2.9$ (left) and $\omega/JS = 3.0$ (right) for the $S = 1/2$ Heisenberg antiferromagnet on the 1393 sites approximant of the octagonal tiling.

In the elastic limit of $S^{\perp}(\mathbf{k},\omega \to 0)$, shown in the left of Fig. 9, we can indeed identify the magnetic Bragg peak positions of the static longitudinal structure factor, shown in Fig. 4. Furthermore, for all energies up to $\omega/JS \approx 2$, similar patterns as in $S^{\perp}(\mathbf{k},0)$ are observed, albeit with the width of the peaks increasing upon increasing the energy. Eventually, these peaks evolve into ring-like structures, centered around the magnetic Bragg peaks, such as shown for $\omega/JS = 1.8$ in the right part of Fig. 9. This is a clear indication for magnetic soft-modes at low energies, which dominate the magnetic response in this energy regime.

Typical examples of $S^{\perp}(\mathbf{k})$ at higher frequencies are shown in Fig. 11, and 12. We find all plots to exhibit an eightfold overall symmetry, as expected for the octagonal tiling. However, the positions of the dominant peaks are different from the magnetic Bragg peaks found below $\omega/JS \approx 2$. For example, for $\omega/JS = 3.0$ (right of Fig. 11), most spectral weight is located at $\mathbf{k} \approx (0, 1.3\pi)$, and $\mathbf{k} \approx (0, 4.3\pi)$, as well as symmetry-related momenta. Peaks at these momenta are absent in both $S^{\parallel}(\mathbf{k},0)$, and

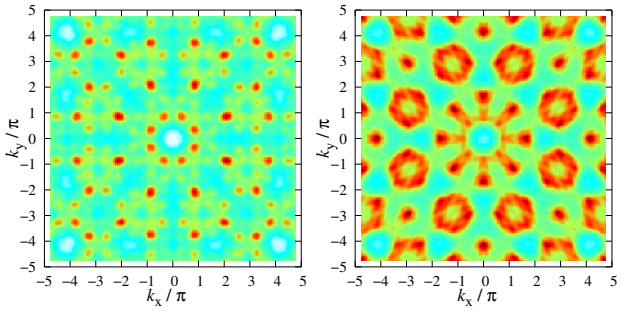

FIG. 12: Intensity plot of the dynamical spin structure factor, $S(\mathbf{k},\omega)$, for fixed $\omega/JS = 4.6$ (left) and $\omega/JS = 6.4$ (right) for the $S = 1/2$ Heisenberg antiferromagnet on the 1393 sites approximant of the octagonal tiling.

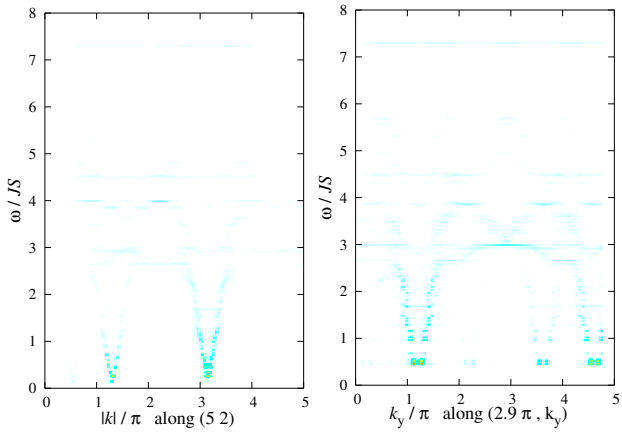

FIG. 13: Intensity plot of the dynamical spin structure factor, $S(\mathbf{k},\omega)$, along the $(5,2)$ momentum space direction (left) and along the line $(2.9\pi, k_y)$ (right) for the $S = 1/2$ Heisenberg antiferromagnet on the 1393 sites approximant of the octagonal tiling.

the nuclear Bragg scattering (Fig. 5 (a) of Ref. 10). In fact, we do not observe pronounced spectral weight at nuclear Bragg peak positions for any finite energy cut: to give a further example of this fact, we show $S^{\perp}(\mathbf{k})$ at $\omega/JS = 4.6$ in the left of Fig. 12. Upon changing the energy-level of the cut only slightly, the patterns found in the high-energy region change more drastically than those in the low-energy regime. As an example, in the left of Fig. 11, we show $S^{\perp}(\mathbf{k})$ for $\omega/JS = 2.9$. Compared to $S^{\perp}(\mathbf{k})$ at $\omega/JS = 3.0$ (right of Fig. 11), we indeed find a different set of dominant peaks.

The patterns in $S^{\perp}(\mathbf{k})$ for energies corresponding to the high-energy pockets in the DOS (c.f. Fig. 6) consist of more diffusive structures than those at lower energies. For example, we find broad ring-like structures, centered around the magnetic Bragg peaks in $S^{\perp}(\mathbf{k})$ for $\omega/JS = 6.4$, shown in the right of Fig. 12. The appearance of such diffusive structures at high energies is expected from the results of Sec. IV B, where the the high-energy excitations were found to be spatially less extended than the low-energy states. This reduced spatial extent leads to smeared diffraction patterns observed in Fig. 12.

In order to analyze the momentum dependence of the dominant peaks in the dynamical spin structure factor, we choose representative directions in momentum space, and plot $S^{\perp}(\mathbf{k},\omega)$ along such cuts. We first consider momenta lying along the (5 2) direction, shown in the left of Fig. 13. This cut passes through two of the major magnetic Bragg peaks, namely at $|\mathbf{k}_B|/\pi \approx 1.3$, and 3.2. In the low-energy region, below $\omega/JS \approx 2$, most spectral weight is located along straight lines, emerging from the magnetic Bragg peaks, and with spectral weight that increases for decreasing energy, characteristic of magnetic soft-modes. Near the magnetic Bragg peaks, $\mathbf{k}_B$, we thus observe linear dispersion relations of the magnetic excitations, $\omega = c|\mathbf{k} - \mathbf{k}_B|$, with an estimated spin-wave velocity $c/JS \approx 2.1$, which is of similar order of magnitude than the linear spin-wave result for the square lattice ($c/JS = \sqrt{8} \approx 2.83$). Similar soft-modes are also observed along the cut of constant $k_x/\pi = 2.9$, shown in the right of Fig. 13, including a further magnetic Bragg peak at $\mathbf{k}_B \approx (2.9\pi, 4.8\pi)$. The emergence of these linear low-energy dispersion relations is consistent with the linear low-energy DOS found in Sec. IV B, and furthermore explains the ring-like structures in $S^{\perp}(\mathbf{k})$, as seen for $\omega/JS = 1.8$ in the right of Fig. 11.

In spite of the absence of translational symmetry, the dynamical spin structure factor of the antiferromagnetic quasicrystal clearly exhibits the presence of soft-modes near the magnetic Bragg peak positions of the quasiperiodic crystal. We expect such a generic feature of magnetic long-range order to be present also in other magnetically ordered quasicrystals.

In contrast, at high frequencies, $\omega/JS > 5.5$, we do not observe any significant dispersion of the spectral weight distribution. Instead, we find two flat bands of only slightly modulated spectral weight located near $\omega/JS \approx 6.4$, and 7.3 in Fig. 14, which correspond to the two isolated pockets of the spin-wave DOS in Fig. 6. We consider this observation as further indication for the limited spatial extent of the corresponding eigenstates, concluded in Sec. IV B from the finite size scaling behavior of the inverse participation ratio.

In the intermediate energy regime, between $\omega/JS \approx 2$, and $\omega/JS \approx 5.5$, the distribution of spectral weight is more complex, and can be accounted for by band-like segments, which recur at different energies and with varying bandwidths, as shown in Fig. 14. At points of increased spectral weight, such as for $\omega/JS = 3$ near $|\mathbf{k}|/\pi \approx 1.8$, and 4.2, in the left of Fig. 14, the corresponding gapped modes furthermore show a linear dispersion relation. In addition, we find bifurcations emerging as branches of these band-segments extending towards low-energies. This is seen for example in the right part of Fig. 14, for momenta $|\mathbf{k}| < \pi$. Such self-similar structures might have been expected to dominate the dynam-

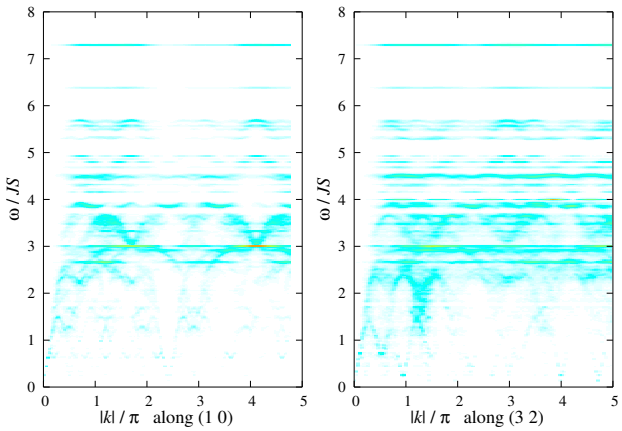

FIG. 14: Intensity plot of the dynamical spin structure factor, $S(\mathbf{k},\omega)$, along the $(1,0)$ momentum space direction (left) and the $(3,2)$ direction (right) for the $S = 1/2$ Heisenberg antiferromagnet on the 1393 sites approximant of the octagonal tiling.

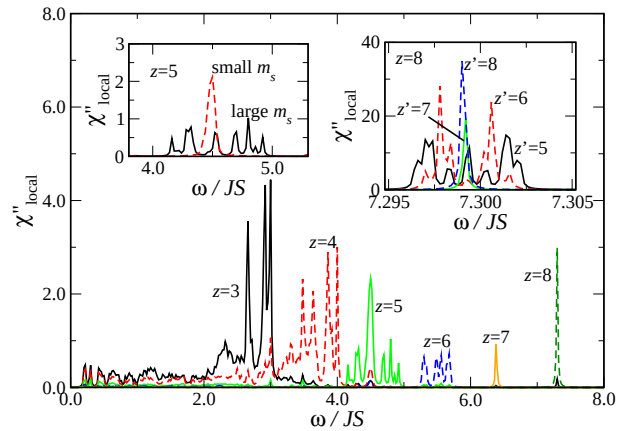

FIG. 15: Imaginary part of the local dynamical spin susceptibility, $\chi''_{local}(i,\omega)$, for the $S = 1/2$ Heisenberg antiferromagnet on the octagonal tiling, averaged separately over sites with coordination numbers $z = 3$ to 8. The left inset shows $\chi''_{local}(i,\omega)$ for the fivefold sites, averaged separately over sites with a small and large staggered magnetization, respectively. The right inset shows $\chi''_{local}(i,\omega)$ for the eightfold sites, averaged separately over sites with different behavior under deflation transformation, grouped according to the value of z'.

ical spin structure factor, due to the geometric properties of the octagonal tiling, reflecting its inflation symmetry. Nevertheless, we find them well separated in energy from more conventional low-energy features, that reflect the magnetic order in this system.

D. Local Dynamical Spin Susceptibility

While the dynamical spin structure factor thus exhibits the peculiar nature of the excitations in the self-similar quasiperiodic system, the different local environments of the magnetic moments in the quasicrystal are accessible from the local dynamical spin susceptibility, the imaginary part of which at each lattice site i is given by

$$\chi''_{local}(i,\omega) = S^{\perp}(i,i,\omega) = S\sum_k \left(|U_{ik}|^2 + |V_{ik}|^2\right)\delta(\omega-\omega_k), \tag{39}$$

within linear spin-wave theory. The local dynamical spin susceptibility is accessible in nuclear magnetic resonance experiments, in the form of Knight-shifts at nuclear sites in the vicinity of the magnetic sites. Here, we study the properties of χ''_{local} for the Heisenberg model on the octagonal tiling, as an example of a quasiperiodic lattice structure.

In Fig. 15, χ''_{local} is shown for the largest approximant, averaged separately for sites of different coordination. We observe a broad spread in the signal, with characteristic energies that increase linearly from $\omega/JS \approx 2.5$ for threefold sites to $\omega/JS \approx 7.3$ for eightfold sites. Furthermore, the energy-range over which there is a large signal narrows for sites of increasing coordination, reflecting a similar trend in the spread of the local staggered moments (c.f. Fig. 3). The inequivalent local environments of the various sites are responsible for this extended range of signals. For example, the left insets of Fig. 15 exhibits that the two types of fivefold sites show a different frequency dependence of the dynamical spin susceptibility. Namely, sites with a smaller moment have signals inside a narrow region near $\omega/JS \approx 4.5$, whereas sites with a larger moment produce signals over a more extended region, ranging from $\omega/JS \approx 4.2$ to $\omega/JS \approx 5$. The high symmetry eightfold sites also exhibit a characteristic splitting in the local spin susceptibility, as seen in the right inset of Fig. 3. Here, the individual signals are labeled by the value of z' for the site from which this signal results. We observe from Fig. 3, that the widths of the signals narrow towards $\omega/JS \approx 7.3$ for increasing values of z'. The local dynamical spin susceptibility thus reflects the hierarchical structure of the local moment distribution of the eightfold sites. We expect such features to be generic properties of quasiperiodic magnets, eventually seen in nuclear magnetic resonance experiments on real quasiperiodic magnetic systems.

V. CONCLUSIONS

We studied the antiferromagnetic spin-1/2 Heisenberg model on the octagonal tiling, a two-dimensional quasiperiodic lattice structure, using linear spin-wave theory in a real space formulation. This approach was found to quantitatively reproduce previous quantum Monte Carlo results on static magnetic ground state properties of this system. The spin-wave excitation spectrum was found to consist of magnon-like low-energy soft-modes with a linear dispersion relation near the magnetic

Bragg peaks, characteristic to long-range magnetic order. It will be interesting to confirm the existence of such linear soft-modes in the octagonal tiling in future quantum Monte Carlo studies of the dynamical spin structure factor.

In addition, the dynamical spin structure factor shows self-similar structures and bifurcations, as well as flat bands at higher energies. We expect such features to be generic to magnetic quasicrystals, which might eventually become observable in neutron scattering experiments on magnetically ordered quasicrystals.

Within the spin-wave approach, it is possible to include magnetic frustration, offering the possibility of modeling more realistic quasiperiodic lattice structures, and their influence on magnetic properties. Starting in the unfrustrated limit, and increasing the magnetic frustration, the evolution of the classical Néel state can be examined, as well as the potential relevance of the multifractal excitations for its breakdown in the case of strong frustration. Another route to magnetic disorder, which can be taken at least theoretically, is by means of a quasiperiodic bilayer, which is expected to show a quantum phase transition upon increasing the interlayer coupling, due to local singlet formation. The presence of multifractal excitations in the quasicrystal might be of possible relevance to quantum criticality in the transition between the Néel ordered state and the disordered, gaped state. We leave such studies for future research.

Acknowledgments

We thank P. Frigeri, S. Haas, O. Nohadani, D. Rau, M. Sigrist, and S. Wehrli for fruitful discussions. The support of the MaNEP project of Swiss National Science Foundation is gratefully acknowledged. Parts of the numerical calculations were done using the ALPS project library[30], and performed on the Asgard Beowulf cluster and Superdome at ETH Zürich.

APPENDIX A: NUMERICAL BOGOLIUBOV TRANSFORMATION

In this appendix we describe an alternative numerical scheme of finding the Bogoliubov transformation of the spin-wave Hamiltonian[31]. We need to construct a matrix T, which diagonalizes the Hamiltonian matrix M defined in Eq. (8), and also satisfies the constraint in Eq. (14). We therefore need to simultaneously solve

$$T^\dagger M T = \Omega, \quad \text{and} \quad T^\dagger \Sigma T = \Gamma. \tag{A1}$$

The matrix T can be constructed in two steps as follows: In a first step, an eigenvector matrix Z and the set of eigenvalues λ_i is obtained for the non-Hermitian eigenvalue problem[22],

$$\Sigma M Z = Z\Lambda, \tag{A2}$$

where $\Lambda = \mathrm{diag}(\lambda_1, \ldots, \lambda_{N_n})$. The columns of Z are the right eigenvectors of ΣM. Hermitian conjugation of the above equation yields

$$(\Sigma Z^\dagger \Sigma)\Sigma M = \Lambda(\Sigma Z^\dagger \Sigma), \tag{A3}$$

so that the rows of $\Sigma Z^\dagger \Sigma$ form the left eigenvectors of ΣM.

In a second step, we diagonalize the Hermitian matrix,

$$L = Z^\dagger \Sigma Z, \tag{A4}$$

obtaining a unitary matrix U, such that

$$U^\dagger L U = \mathrm{diag}(l_1, \ldots, l_{N_n}). \tag{A5}$$

Furthermore, from the eigenvalues l_i of L we construct the diagonal matrix $l^{-1/2}$, defined as

$$l_{ij}^{-1/2} = \delta_{ij}|l_i|^{-1/2}. \tag{A6}$$

In case that the eigenvalues of ΣM are non-degenerate, performing this second step is trivial: In this case l_i is the Σ-norm of the corresponding eigenvector, and $U = 1$. We finally obtain the transformation T as:

$$T = ZUl^{-1/2}. \tag{A7}$$

Indeed, since

$$\bar{\Gamma} = T^\dagger \Sigma T \tag{A8}$$

satisfies $\bar{\Gamma}^2 = 1$ by construction, T satisfies the constraint Eq. (14). Furthermore, right and left eigenvectors belonging to different eigenvalues are orthogonal. Thus L is block diagonal with blocks corresponding to degenerate subspaces of ΣM. It follows that U is block diagonal as well. Therefore U only mixes columns of Z belonging to the same eigenvalue of ΣM, and consequently T satisfies

$$\Sigma M T = T\bar{\Lambda}. \tag{A9}$$

Multiplying the above equation from the left by $T^{-1} = \Gamma T^\dagger \Sigma$ (which follows from Eq. (A8)), yields

$$T^\dagger M T = \Lambda\bar{\Omega}. \tag{A10}$$

Hence, the matrix T also diagonalizes the Hamiltonian matrix M. The energies of the bosonic eigenmodes are given as $\omega_i = JS\Gamma_{ii}\lambda_i$, respectively.

[1] E. Manousakis, Rev. Mod. Phys. **63**, 1 (1991), and references therein.
[2] A. Koga, S. Kumada, N. Kawakami, J. Phys. Soc. Jpn. **68** (7), 2373 (1999).
[3] A. Läuchli, S. Wessel, and M. Sigrist, Phys. Rev. B **66**, 014401 (2002).
[4] Gregoire Misguich, Claire Lhuillier, Report cond-mat/0310405, and references therein.
[5] A. Sandvik, Phys. Rev. B **66**, 024418 (2002).
[6] E. R. Mucciolo, A. H. Castro Neto, and C. Chamon, Report cond-mat/0402102.
[7] T. J. Sato, H. Takakura, A. P. Tsai, K. Shibata, K. Ohoyama, and K. H. Andersen, Phys. Rev. B **61**, 476 (2000).
[8] T. J. Sato, H. Takakura, G. Guo, A. P. Tsai, and K. Ohoyama, J. of Alloys and Compounds, **342**, 365 (2002).
[9] T. J. Sato, H. Takakura, A. P. Tsai, and K. Shibata, Phys. Rev. Lett. **81**, 2364 (1998).
[10] S. Wessel, A. Jagannathan, S. Haas, Phys. Rev. Lett. **90**, 177205 (2003).
[11] A. Jagannathan, Phys. Rev. Lett. **92**, 047202 (2004).
[12] R. Lifshitz and S. Even-Dar Mandel, Acta Cryst. A **60**, 167 (2004).
[13] Ron Lifshitz, Material Science and Engineering A **294**, 508 (2000).
[14] E. Y. Vedmedenko, U. Grimm, and R. Wiesendanger, Report cond-mat/0406373.
[15] U. Grimm, and M. Schreiber, in *Quasicrystals - Structure and Physical Properties*, ed. H.-R. Trebin (Wiley-VCH, Weinheim, 2003), and references therein.
[16] D. Levine and P. J. Steinhardt, Phys. Rev. B **34**, 596 (1986).
[17] R. M. White, M. Sparks, and I. Ortenburger, Phys. Rev. **139**, 450 (1965).
[18] M. Duneau *et al.*, J. Phys. A **22**, 4549 (1989).
[19] A. Jagannathan and H. J. Schulz, Phys. Rev. B **55**, 8045 (1997).
[20] K. Yosida, *Theory of Magnetism* (Springer, 1996).
[21] J.-P. Blaizot and G. Ripka, *Quantum Theory of Finite Systems* (MIT Press, Cambridge, MA, 1986).
[22] Using standard numerical routines, for example from LAPACK.
[23] S. Lang, *Algebra*, (3rd Edition, Addison-Wesley 1993).
[24] T. Einarsson and H. J. Schulz, Phys. Rev. B **51**, 6151 (1995).
[25] S. Wessel, unpublished.
[26] We verified, that the shown averages are indeed representative of the individual contributions.
[27] A. Jagannathan, Phys. Rev. B. **61**, R834 (2000).
[28] F. Wegner, Z. Phys. B **36**, 209 (1980).
[29] M. Schreiber and H. Gurssbach, Phys. Rev. Lett. **67**, 607 (1991).
[30] M. Troyer *et al.*, Lecture Notes in Computer Science **1505**, 191 (1998). Source codes of the library can be obtained from `http://alps.comp-phys.org/` .
[31] Avery J. *Creation and annihilation operators* (McGraw-Hill, 1974), appendix 1 and references therein.